metals

MDPI

Article

Effect of Yttrium and Yttria Addition in Self-Passivating WCr SMART Material for First-Wall Application in a Fusion Power Plant

Jie Chen [1,*], Elena Tejado [2], Marcin Rasiński [1], Andrey Litnovsky [1], Duc Nguyen-Manh [3], Eric Prestat [3], Tamsin Whitfield [3], Jose Ygnacio Pastor [2], Martin Bram [4], Jan Willem Coenen [1], Christian Linsmeier [1] and Jesus Gonzalez-Julian [4,5]

1 Institute of Fusion Energy and Nuclear Waste Management, Plasma Physics (IFN-1), Forschungszentrum Jülich GmbH, D-52425 Jülich, Germany
2 Departamento de Ciencia de Materiales-CIME, Universidad Politécnica de Madrid, E-28040 Madrid, Spain
3 Culham Centre for Fusion Energy, Culham Campus, United Kingdom Atomic Energy Authority, Abingdon OX14 3DB, UK
4 Institute of Energy Materials and Devices, Materials Synthesis and Processing (IMD-2), Forschungszentrum Jülich GmbH, D-52425 Jülich, Germany
5 Institute of Mineral Engineering, RWTH Aachen University, D-52074 Aachen, Germany
* Correspondence: ji.chen@fz-juelich.de

Abstract: The self-passivating yttrium-containing WCr alloy has been developed and researched as a potential plasma-facing armour material for fusion power plants. This study explores the use of yttria (Y_2O_3) powders instead of yttrium elemental powders in the mechanical alloying process to assess their applicability for this material. Fabricated through field-assisted sintering, WCr-Y_2O_3 ingots show Y_2O_3 and Cr-containing oxides (Cr-O and Y-Cr-O) dispersed at grain boundaries (GBs), while WCrY ingots contain Y-O particles at grain boundaries, both resulting from unavoidable oxidation during fabrication. WCr-Y_2O_3 demonstrates higher flexural strength than WCrY across all temperature ranges, ranging from 850 to 1050 MPa, but lower fracture toughness, between 3 and 4 MPa·$\sqrt{m}$. Enhanced oxidation resistance is observed in WCr-Y_2O_3, with lower mass gain as compared to WCrY during the 20-hour oxidation test. This study confirms the effectiveness of both yttria and yttrium in the reactive element effect (REE) for the passivation of WCr alloy, suggesting the potential of Y_2O_3-doped WCr for first wall applications in a fusion power plant.

Keywords: self-passivating; yttrium; plasma-facing; yttria; flexural strength; fracture toughness; oxidation resistance

Citation: Chen, J.; Tejado, E.; Rasiński, M.; Litnovsky, A.; Nguyen-Manh, D.; Prestat, E.; Whitfield, T.; Pastor, J.Y.; Bram, M.; Coenen, J.W.; et al. Effect of Yttrium and Yttria Addition in Self-Passivating WCr SMART Material for First-Wall Application in a Fusion Power Plant. *Metals* **2024**, *14*, 1092. https://doi.org/10.3390/met14091092

Academic Editor: Arne Mattias Thuvander

Received: 30 August 2024
Revised: 18 September 2024
Accepted: 21 September 2024
Published: 23 September 2024

1. Introduction

Tungsten (W) is currently considered the prime candidate for the first wall material in future fusion reactors due to its exceptional properties, including the highest melting point among metals, high-temperature strength, good thermal conductivity, and low plasma erosion yield [1]. However, a potential loss-of-coolant accident (LOCA) event, accompanied by air and/or water leaking into the vacuum vessel due to mechanical damage, could result in the temperature rise of a tungsten-made first wall to 1000 °C or higher and simultaneous oxidation [2]. Tungsten oxide is volatile at such temperatures, and the release of aerosols containing radioactive oxide WO_3 into the atmosphere is a concern [3]. This leads to research into self-passivating metal alloys with reduced thermo-oxidation (SMART) as an alternative to plasma-facing materials in, e.g., the DEMOnstration power plant (DEMO) [4,5]. Beyond maintaining acceptable plasma performance during regular operation, SMART materials must demonstrate suppressed oxidation of tungsten by forming dense and thermally stable oxide scales of the passivating alloying elements during the abovementioned accidental event, ensuring passive safety for tungsten-based first wall

applications. Recent research has been conducted investigating various aspects of SMART materials, including manufacturing [6–9], fuel retention [10–12], the neutron-irradiation effect [13], microstructural stability [14], the materials' response in fusion conditions [15], joining [16], and surface analysis [17,18].

Based on tungsten, modern SMART materials incorporate 10–12 wt.% Cr as the passivating element and <1 wt.% Y as the so-called reactive element (RE). The addition of ~0.6 wt.% Y has demonstrated a reduced oxidation rate by at least one order of magnitude compared to the W-Cr binary alloy [3,19]. Moreover, Y addition has also been proven effective in enhancing oxidation resistance in W-Si-Y [20,21]. Yttrium as RE is widely recognized for the following three primary effects (reactive element effect, REE) that contribute to improved oxidation resistance [22,23]: (1) promoting selective oxidation and reducing the amount of Cr or time required to establish chromia scales [24]; (2) impeding outward diffusion of metal cations as segregating elements in GBs and thus altering the growth process of chromia scales [25]; and (3) enhancing the scale adherence to base metal and reducing the likelihood of spallation [26]. However, when added in elemental form, yttrium is found inevitably oxidized as particles mainly dispersed in GBs of WCr alloys, whether fabricated through field-assisted sintering technology (FAST) [27] or hot isostatic pressing (HIP) [28]. This is attributed to the strong oxygen affinity of elemental yttrium, as well as other REs such as Zr [29], Ti [30], and Hf [31], which are also observed in the form of oxides after the fabrication of WCr alloys.

The oxidation of elemental yttrium during manufacturing suggests the alternative approach of adding yttria, its oxide form, to the WCr alloy directly. Research on the addition of yttria to WCr alloys is limited compared to the extensively studied WCrY system. However, the role of yttria as the RE oxide during oxidation and its impact on mechanical properties warrant exploration. Yttria has been studied in chromia-forming Fe-based [32] and Ni-based [33,34] alloys exhibiting similar functionalities to yttrium during oxidation. Additionally, numerous investigations have shown that the addition of yttria to pure tungsten leads to mechanical improvement [35–38]. This work, therefore, initiates the substitution of yttrium with yttria in WCr alloy and compares the oxidation performance of samples at an isothermal temperature of 1000 °C, as well as their thermo-mechanical properties, to evaluate their potential use in first wall applications.

It is worth emphasizing that the nuclear response of W-based SMART materials has been considered under conditions expected for first wall components in DEMO for two years of continuous full-power operations [39,40]. The inventory code FISPACT-II [41] was used to predict changes in composition due to transmutation as well as the compositional evolution after irradiation during decay cooling and subsequently derive the total activity of the materials. These studies demonstrate that W suffers the most severe transmutation, potentially growing several atomic percent, whereas the alloying elements (Ti, Cr, Y, and Zr) show at least an order of magnitude lower transmutation rates. It is also worth mentioning that as the first wall material, whether the intentional addition of oxygen in SMART materials is compatible with the potential start-up problem in DEMO requires future investigation.

2. Materials and Methods

For sample preparation, elemental powders W (99.9%, 4 μm), Cr (99.7%, 45 μm), and Y (99.9%, 500 μm), as well as Y_2O_3 nanopowders (99.99%, 29 nm) were used as raw materials. Two initial powder batches, each weighing 110 g, were prepared with nominal compositions of W-11.4Cr-0.6Y and W-11.4Cr-0.76Y_2O_3 (in wt.%), respectively. These compositions are expressed as weight percentage (wt. %) and contain an equal atomic percent of yttrium element (~0.96 at.%) and chromium element (~31.1 at.%). Both batches were ground for 60 h in a planetary mill (Retsch PM400 MA, Retsch GmbH, Haan, Germany) under an argon atmosphere, with a milling rotation speed of 198 rotations per minute (rpm) and a ball-to-powder weight ratio of 5:1. Subsequently, the alloyed powders were consolidated at 1460 °C with a heating rate of 200 °C/min using FAST equipment (FCT-HPD5, FCT

Systeme GmbH, Rauenstein, Germany). No isothermal holding was performed during the sintering process. A uniaxial pressure of 50 MPa was applied to the green compact of powders, and a vacuum atmosphere was maintained during sintering. The resulting cylindrical ingots had a diameter of Ø20 mm and a mass of 25 g.

For as-sintered ingots, the microstructures of lamellar specimens (prepared by focused ion beam) were characterized using the scanning transmission electron microscopy (STEM) mode in scanning electron microscope (SEM) (Zeiss Crossbeam XB 540, Carl Zeiss Microscopy GmbH, Jena, Germany). The average grain size, average size, and number density of oxide particles in secondary electron (SE) images were evaluated using ImageJ software Version 1.53k [42]. The lattice parameters of WCrY and WCr-Y_2O_3, both in the form of as-milled powders and as-sintered ingots, were determined based on (110), (200), and (211) peaks in X-ray diffraction (XRD) patterns. XRD analysis was conducted by scanning from 20° to 120° (2θ) with an increment of 0.02° using a D8 Discover from Bruker AXS GmbH. The incident beam was Cu Kα X-rays. For as-oxidized samples, SE images of cross-sectional and surface microstructures were taken using the focused ion beam scanning electron microscope (FIB-SEM, the same device mentioned above). Chemical analyses of oxide particles in the as-sintered samples and various regions in as-oxidized samples were performed using energy-dispersive X-ray spectroscopy (EDS, Oxford Instruments plc, Abingdon, Oxfordshire, UK) operating at an accelerating voltage of 12 kV. The W M_α, Cr K_α, Y L_α, and O K_α lines were chosen for analysis.

For oxidation testing, cuboidal samples (approximately 4.9 × 2.8 × 3.8 mm) were machined from as-sintered ingots using electrical discharge machining (EDM) and subsequently ground to a 1200-grit SiC paper. Oxidation experiments lasting 20 h were conducted in a thermogravimetric analyser (TGA, TAG-16, Setaram Inc., Caluire-et-Cuire, France) at 1000 °C under a gas mixture of N_2 + 20 vol.% O_2, with a relative humidity of 70% at 25 °C and a gas flow rate of 40 mL/min.

For mechanical characterization, Vickers hardness (HV 0.5) was performed on as-polished ingots using DuraScan G5 (ZwickRoell GmbH & Co. KG, Ulm, Germany), applying a load-dwelling time of 10 s. Three-point bending (TPB) tests were carried out on both unnotched and single edge laser-notched beams, with nominal dimensions of 20 × 2.1 × 1.4 mm, to measure flexural strength and fracture toughness, respectively. These tests were carried out using an Instron 8862 universal testing machine (Instron, UK), spanning temperatures from 25 °C to 1100 °C under high-vacuum conditions (10^{-6} mbar) and 10 min stabilization time. All tests were performed under displacement control at a constant loading rate of 100 µm/min, with a 12 mm span length. Fracture toughness (K_{IQ}) was determined using the formula proposed by Pastor and Guinea et al. [43,44].

3. Results and Discussion

3.1. Microstructures

The primary microstructural difference between as-sintered WCrY and WCr-Y_2O_3 lies in the composition of oxide particles at GBs. In as-sintered WCrY, only Y-O particles are detected, regardless of particle size (Figure 1a), suggesting inevitable oxidation during fabrication despite inert gas milling and vacuum sintering. Oxygen impurities in raw elemental powers or residual oxygen in the milling jar and the sintering chamber may contribute to oxide formation. In as-sintered WCr-Y_2O_3, the mixture particles composed of Cr-O and Y-Cr-O are mainly observed (Figure 1b). This indicates that the Cr-involving reaction occurs during manufacturing, which is not observed in the WCrY system, and that there is a transformation of Y_2O_3 into Y-Cr-O. The stoichiometry of oxides (Y-O in WCrY, Cr-O, and Y-Cr-O in WCr-Y_2O_3) has not been confirmed in this study. For the Y-Cr-O compound, $YCrO_3$ is the stable form and belongs to the space group Pnma (62) with a = 5.524 Å, b = 7.534 Å, c = 5.243 Å, and angles $\alpha = \beta = \gamma = 90°$ [45]. Our first-principles calculations predicted a stable $YCrO_3$ compound with the enthalpy of formation of −1354.03 kJ/mol compared to −1746.24 kJ/mol for Y_2O_3. These calculations were performed using density functional theory (DFT) as implemented in the VASP package using the PBE exchange-correlation

functionals [46–48]. Standard projector augmented wave (PAW) pseudopotentials were employed throughout this study with a plane-wave cut-off energy of 520 eV. In all cases, the k-point grids were converged to ensure a maximum error of 1 meV per atom. $YCrO_3$ can be formed through the following reaction: $Cr + 0.75O_2 + 0.5Y_2O_3 = YCrO_3$, starting at ~1100 °C, as observed in some dedicated experiments [49]. Ref. [50] shows that Y_2O_3 additives transform to $YCrO_3$ in Ni-Cr-Y_2O_3 ingots when the sintering temperature reaches 1100 °C. Other research suggests the presence of the Y-Cr-O compound after sintering mechanically alloyed powder with Y_2O_3 addition in Fe-based [51] and Co-based [52] alloys, also processed at 1100 °C. We thereby suggest that Y-Cr-O oxides in our work form during the sintering stage where the necessary temperature for reaction is achieved. Moreover, the lattice parameter slightly increases after sintering WCr-Y_2O_3 powders (Table 1), implying minor Cr depletion in the solid solution of WCr. This indirectly indicates the reaction of Cr with O and Y_2O_3 particles to form Cr-O as well as Y-Cr-O compounds during sintering. However, the overall depletion of Cr after sintering is minimal, as the Cr content (28.4 at.% measured by EDS) within grain interiors still remains close to the nominal composition (31.1 at.%). Further research shows that Y_2O_3 has already partially transformed into $YCrO_3$ in small amounts in Ni-Cr-Y_2O_3 powders in the as-milled state, but a high-number density of $YCrO_3$ precipitated after hot isostatic pressing at 1175 °C [53], suggesting that consolidation at high temperature is the dominant process for $YCrO_3$ formation compared to ball milling. Noticeably, a lower temperature of 1000 °C for the formation of $YCrO_3$ during heat treatment has been reported in a mixture of Y_2O_3-Cr_2O_3 powders, but this process has slow kinetics, as Y_2O_3 and $YCrO_3$ still coexist after an exposure of 12 days [54]. Similarly, in Fe-Cr-Y_2O_3 powders, Y_2O_3 and $YCrO_3$ coexist after an exposure of 1 h at 1000 °C [55]. Given the fast processing of WCr-Y_2O_3 during sintering (heating stage of 5 min to 1460 °C without isothermal), 1000 °C is a less-likely onset temperature for formation of Y-Cr-O compared to 1100 °C or above in this study, due to the limited reaction time.

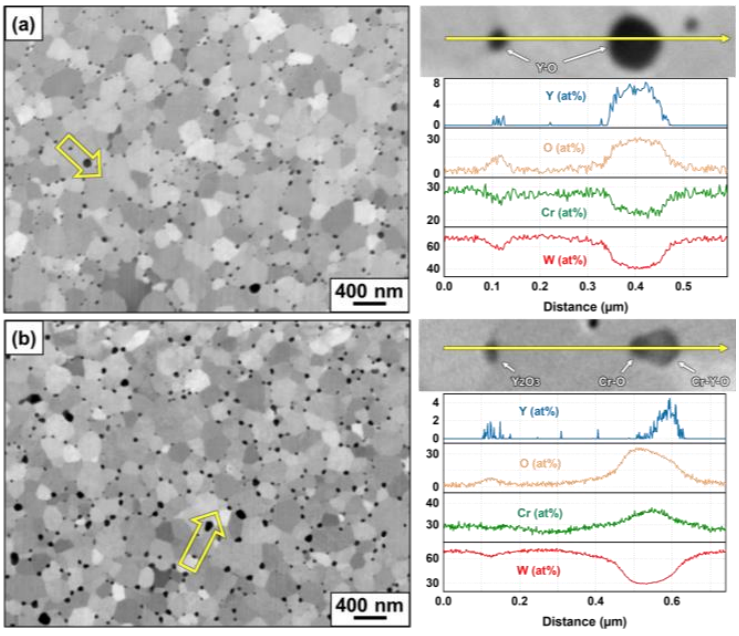

Figure 1. STEM microstructures of as-sintered (**a**) WCrY and (**b**) WCr-Y_2O_3 on the left, and corresponding EDS line scan across oxides of different sizes on the right. The yellow arrows on the left side indicate the locations where EDS line scan results are made and shown on the right side.

Table 1. Microstructural features of WCr-Y_2O_3 and WCrY (average grain size d_g, average diameter d_p, area number density ρ_N of oxide particles, lattice parameter a, and micro-hardness (HV 0.5)).

Composition	d_g (nm)	d_p (nm)	ρ_N (m^{-2})	a (Å)		HV 0.5
				As-Milled Powder	As-Sintered Ingot	
WCrY	183 ± 18	33 ± 17	2.2×10^{13}	3.098	3.099	1207 ± 9
WCr-Y_2O_3	200 ± 12	42 ± 21	2.0×10^{13}	3.097	3.102	1135 ± 9

In contrast to WCr-Y_2O_3, the as-sintered WCrY does not exhibit a noticeable Cr-involving reaction. This aligns with findings from Ref. [56], which report the formation of Y_2O_3 in Ni-Cr-Y and $YCrO_3$ in Ni-Cr-Y_2O_3 after FAST sintering. The Gibbs energies of formation for these oxides are estimated as follows: Y_2O_3 < Cr_2O_3 < $YCrO_3$ (using Y_2O_3 as the reactant, 1100–1700 K) [57,58]. The strong affinity of yttrium for oxygen makes it the dominant oxygen getter in the WCrY system. However, the Y-O particles in the WCrY system might be non-stoichiometric. In the WCr-Y_2O_3 system, elemental Cr serves as the oxygen scavenger due to the absence of elemental Y. The oxidation of Cr has been reported at temperatures of 700 °C or even lower [59–61]. Therefore, it is suggested in WCr-Y_2O_3 that Cr-O precipitates likely form in GBs in the early heating stage of sintering (e.g., <1100 °C). These Cr-O particles could become the preferential nucleation sites for Y-Cr-O when sintering proceeds to higher temperatures (e.g., 1100 °C or above), which explains why Y-Cr-O is often seen adjacent to Cr-O. The Cr-involving reactions in the WCr-Y_2O_3 system may account for the increased size of oxide particles, which are approximately 20% larger, on average, compared to those in WCrY (Table 1). A small fraction of the original Y_2O_3 additives appears to be unreacted, thus retaining the small size, as shown in the EDS result in Figure 1b. The overall larger dispersoids with lower number density in WCr-Y_2O_3 do not inhibit grain growth as effectively as their smaller counterparts in WCrY, leading to slightly larger grain size and reduced hardness.

3.2. Oxidation Tests

The mass change curves of the two materials and pure W over a 20 h period are presented in Figure 2. Both materials exhibit significantly lower oxidation rates compared to pure W. WCrY oxidizes at a linear rate of 1.1×10^{-5} mg·cm^{-2}·s^{-1}, consistent with previous work under identical oxidation conditions [62]. Substituting Y with Y_2O_3 reduces the linear oxidation rate of WCr-Y_2O_3 by roughly half to 5.7×10^{-6} mg·cm^{-2}·s^{-1}. The two materials exhibit different surface conditions after oxidation. The oxidized WCrY surface (Figure 3a) consists of (a) mixed-oxide areas (the chromia scale covered by Y-containing particles), (b) bare chromia areas, and (c) the "disrupted regions". These disrupted regions have undergone more intense oxidation, leading to a greater amount of tungsten oxide formation compared to other areas. Tungsten oxides (WO_3) are volatile at 1000 °C, and their increased formation enhances the likelihood of sublimation from below the surface. This sublimation could disrupt the passivating layer, resulting in the formation of the observed structures and, thus, the discontinuities of the oxide scale on the surface. In contrast, the oxidized WCr-Y_2O_3 surface (Figure 3d) shows a more uniform distribution of Y-containing particles on the chromia scale, significantly reducing the occurrence of bare chromia areas and disrupted regions. According to EDS analysis in Figure 3b,e, the Y-rich particles in both oxidized materials suggest the presence of $YCrO_3$ particles (blue, marked as 1 and 4) based on the atomic ratio of Y and Cr, and Y-Cr-W-O particles (red, marked as 2 and 5). The quantity of Y-Cr-W-O particles is higher compared to $YCrO_3$ particles. The remaining oxide (green) is pure chromia. Cross-section views (Figure 3c,f) show layered structures with the chromia scale on top and the inner oxide layer in both materials. Notably, WCr-Y_2O_3 features a chromia layer nearly twice as thick (1161 ± 605 nm) as WCrY (646 ± 431 nm) and a shallower inner oxide layer (3.1 ± 0.5 µm) compared to WCrY (4.0 ± 0.6 µm). The inner oxide layer contains W-Cr-O in the upper region and tungsten oxides in the lower region. Hence, from the reduced presence of disrupted regions, decreased thickness of the inner

oxide layer, and lower mass gain, it can be said that WCr-Y_2O_3 shows further enhanced oxidation resistance compared to WCrY.

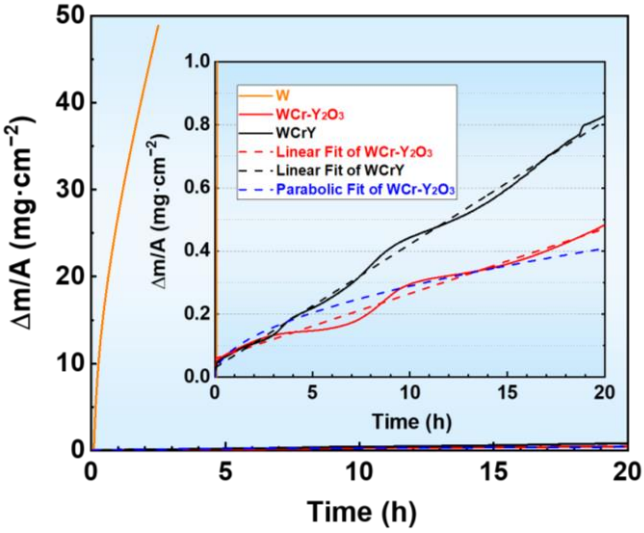

Figure 2. Mass change of pure W, WCrY, and WCr-Y_2O_3 under synthetic air and isothermal temperature of 1000 °C, as a function of time (20 h in total). The inset highlights a smaller scale on the *y*-axis. The R-squared is 0.9960 for linear fitting of WCrY, 0.9826 for linear fitting of WCr-Y_2O_3, and 0.9101 for parabolic fitting of WCr-Y_2O_3.

The passivation behaviour in both Y- and Y_2O_3-doped WCr alloys demonstrates that REE (as described in the introduction) can occur when yttrium is present in various forms in the as-sintered materials: Y-O or Y-Cr-O. In WCrY alloys containing Y-O particles, the oxidized surface features areas without Y-containing particles, including bare chromia areas and disrupted regions. In contrast, WCr-Y_2O_3 alloys with Y-Cr-O particles display a uniform distribution of Y-containing particles across the oxidized surface. The exact mechanism by which different yttrium oxide formed in as-sintered materials influences the homogeneity of Y-rich particles on the oxidized surface is not fully understood. Nevertheless, the enhanced passivation observed in WCr-Y_2O_3 suggests that the Y-Cr-O particles provide a more effective REE during oxidation compared to Y-O particles. This may be related to the evolution of yttrium during oxidation, proposed in the following sequence: Y (elemental form) → Y-O (non-stoichiometric) → Y_2O_3 → Y-Cr-O (non-stoichiometric) → $YCrO_3$. It is often reported in the chromia formers that Y or Y_2O_3, introduced through alloying [63], oxide dispersion [64], ion implantation [65,66], or coating [67,68], react with Cr to form $YCrO_3$ during high-temperature corrosion tests, and $YCrO_3$ typically appears along the scale boundary. For instance, Ref. [65] presents the evolution of implanted Y in Co-Cr alloy oxidized at 1000 °C, with most of the Y present as Y_2O_3 after the first 4 h of oxidation and then transforming into $YCrO_3$ particles after 24 h. After its formation, the presence of $YCrO_3$ at the scale/substrate interface can improve the scale adherence. Additionally, $YCrO_3$ is in a thermodynamically stable phase in air up to its melting point of 2300 °C [67], but it begins to dissociate at the partial oxygen pressure of ~10^{-25} bar at 1000 °C [57], releasing Y ions that segregate at the oxide scale's GBs [66,69]. Therefore, REE is associated with the formation of $YCrO_3$ [70]. However, since Y-O particles are present in as-sintered WCrY, the formation of stoichiometric Y_2O_3 and, subsequently, $YCrO_3$ during oxidation could be a precursor to REE. The transformation of Y_2O_3 into $YCrO_3$ is a relatively slow process at 1000 °C, as noted in Ref. [54]. In contrast, the pre-existing Y-Cr-O oxides in as-sintered WCr-Y_2O_3 bypass the evolution of Y and thereby enhance the material's readiness for REE in response to oxidation.

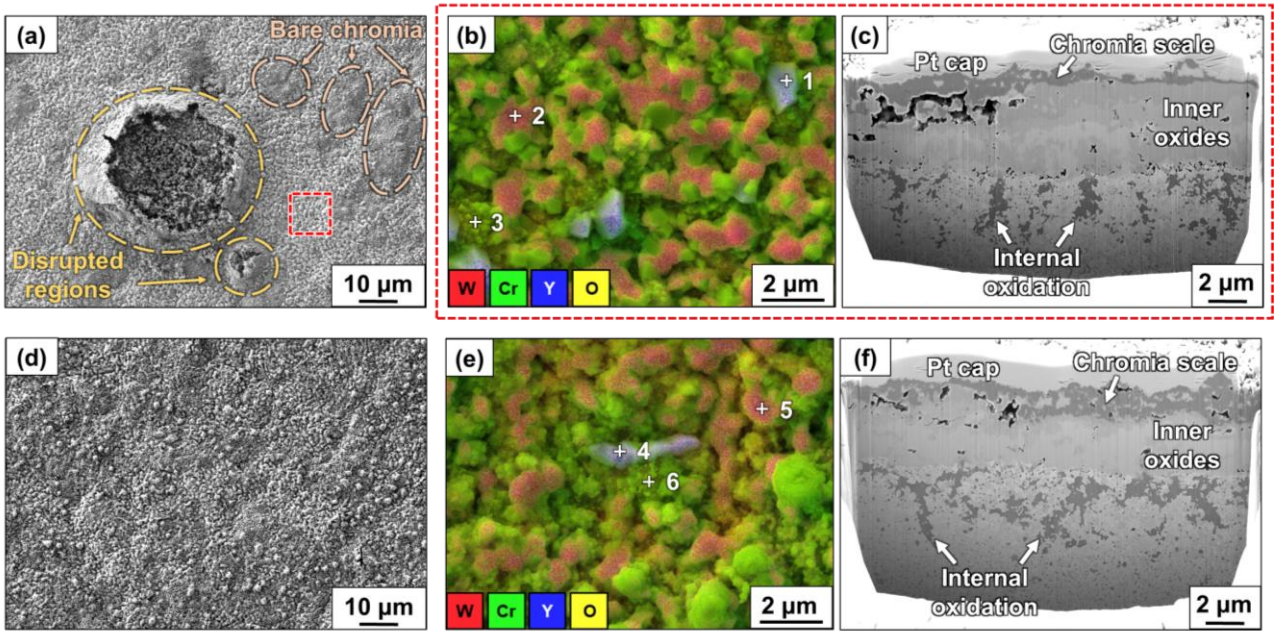

	1	2	3	4	5	6
Y	12.9	8.1	-	12.6	5.9	-
Cr	12.9	17.5	35.9	12.5	14.6	36.7
W	1.4	12.9	2.8	1.6	10.5	2.1
O	72.9	61.5	61.3	73.3	68.9	61.2

Figure 3. (**a**) The oxidized surface of WCrY, consisting of disrupted regions, bare chromia areas, and mixed-oxide areas (Y-rich oxides on chromia scale). The red box indicates an example of a mixed-oxide area.(**b**) EDS layered mapping of the mixed-oxide area of WCrY. (**c**) Cross-section under the mixed-oxide area of WCrY. (**d**) The oxidized surface of WCr-Y_2O_3 consisting of solely mixed-oxide areas. (**e**) EDS layered mapping of the mixed-oxide area of WCr-Y_2O_3. (**f**) Cross-section under the mixed-oxide area of WCr-Y_2O_3. The table shows the chemical composition (in at.%) of different oxides on the surface, detected by EDS point analysis. Three species of oxides are shown in both (**b**,**e**): red (marked as 2 and 5) is Y-Cr-W-O, blue (marked as 1 and 4) is $YCrO_3$, and green (marked as 3 and 6) is Cr_2O_3.

3.3. Three-Point Bending Tests

The flexural stress—strain curves of both materials at varying temperatures are given in Figure 4a,b. WCr-Y_2O_3 exhibits a slightly higher ductile—brittle transition temperature (DBTT), with WCr-Y_2O_3 beginning to show ductility at 950 °C and WCrY at 900 °C. This could be attributed to the larger grain size of WCr-Y_2O_3. Clear plastic deformation appears in both materials above 1000 °C. The fractured surface at room temperature shows predominantly intergranular cracking for WCrY and a mixed-fracture mode (intergranular cracking and cleavage through grains) for WCr-Y_2O_3, as shown in Figure 4c,d.

Figure 5a illustrates the proof flexural strength of both materials as a function of temperature. Both materials maintain their flexural strength from room temperature to 900 °C, with a slight decrease observed both at 600 °C and 800 °C. WCr-Y_2O_3 consistently shows higher strength than WCrY at all test temperatures, although the difference narrows at higher temperatures. At room temperature, WCr-Y_2O_3 exhibits a flexural strength of ~1 GPa, which is 40% higher than WCrY. However, this difference is minimal (9%) at 600 °C. The greater strength of WCr-Y_2O_3 suggests that its fewer and larger oxide particles (and thus further interparticle spacing) at GBs provide more strengthening compared to the more numerous and smaller counterparts in WCrY. Meanwhile, the different coherence of the Y-Cr-O and Y-O particles with the (αW, Cr) matrix may also play a role, with Y-Cr-O possibly providing greater resistance to dislocation motion.

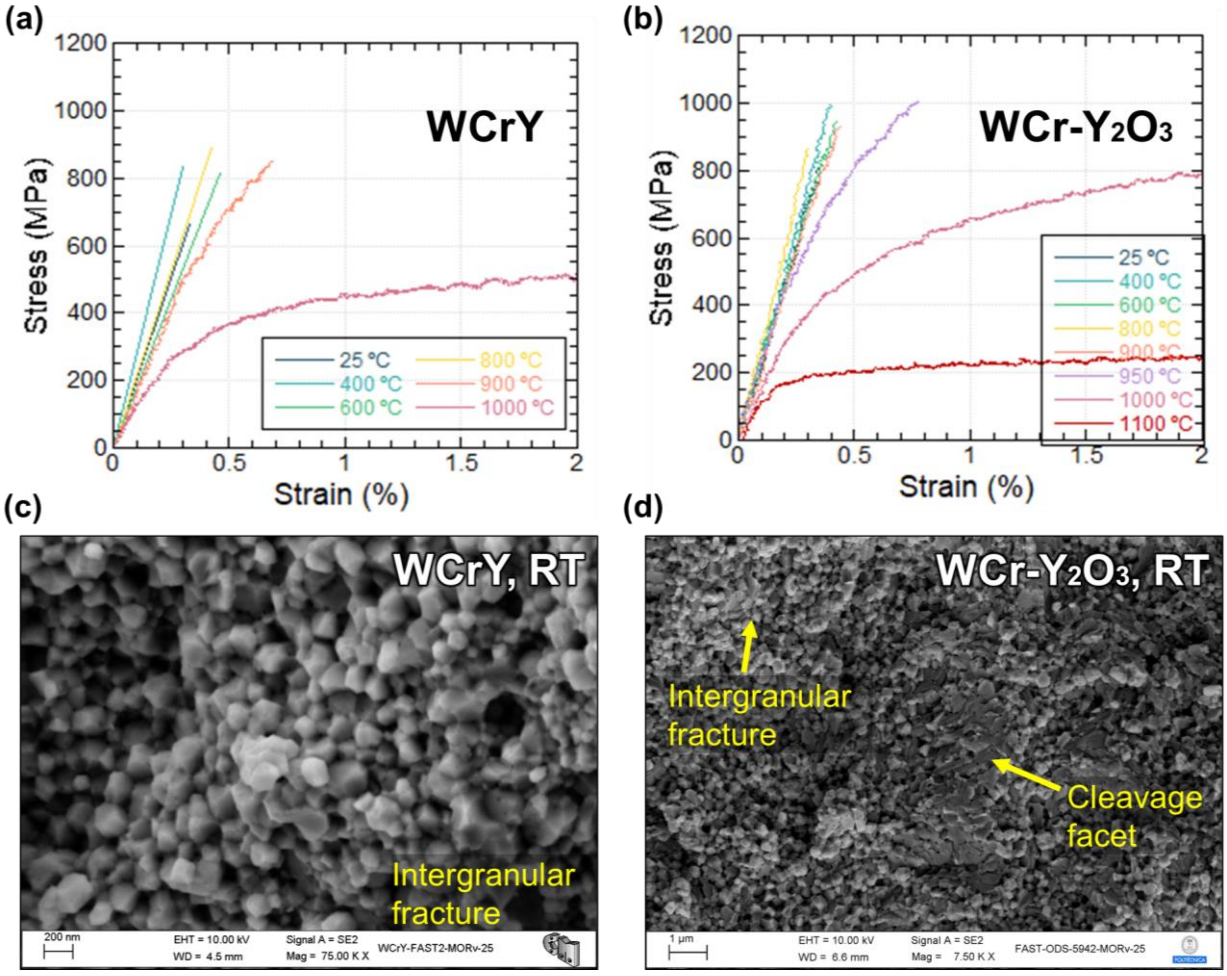

Figure 4. Flexural stress vs. strain from 25 °C to high temperatures of (**a**) WCrY and (**b**) WCr-Y_2O_3. Fracture surface of (**c**) WCrY and (**d**) WCr-Y_2O_3, respectively (materials fractured at room temperature). An additional test at 950 °C was conducted for WCr-Y_2O_3 to see if the material exhibited ductility before proceeding with the test at 1000 °C.

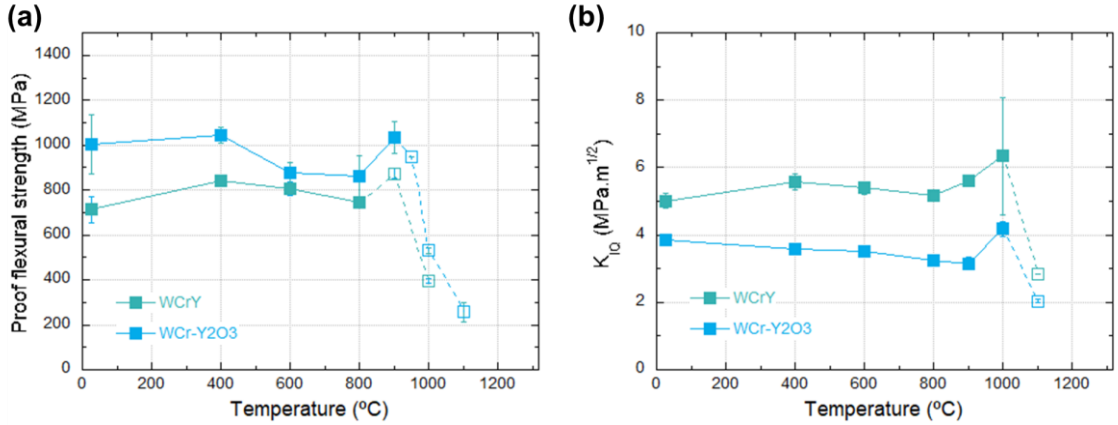

Figure 5. (**a**) Flexural strength and (**b**) fracture toughness of WCrY and WCr-Y_2O_3 at varying temperatures. Closed symbols and solid lines denote the ultimate flexural strength or K_{IQ} values based on the maximum load upon brittle fracture. Open symbols and dashed lines denote yield flexural strength $\sigma_{0.2}$ or K_{IQ} values based on the 5% secant line when non-linear behaviour was observed. Both flexural strength and fracture toughness are calculated as the average of at least two measurements, with the error bars representing the standard error.

In contrast, the fracture toughness of WCr-Y_2O_3 is lower overall than that of WCrY across all test temperatures, measuring 3~4 MPa·$\sqrt{m}$ compared to 5~6 MPa·$\sqrt{m}$. The fracture toughness of WCr-Y_2O_3 continuously decreases as temperature increases to 900 °C. The low fracture toughness of both materials is partly attributed to weak grain boundary cohesion and embrittlement of oxide particles at GBs. However, the reduced toughness in WCr-Y_2O_3 materials indicates that Y-Cr-O particles may have a further embrittlement effect than Y-O particles, promoting both intergranular and transgranular crack propagation, as observed in Figure 4d. Coarser particles tend to create higher stress/strain concentrations and trigger interfacial decohesion at weaker grain boundaries [71,72]. They are also more prone to breakage due to their lower fracture strength, as the fracture strength of these particles decreases with increasing particle size [73]. This could explain why the presence of larger oxide particles in WCr-Y_2O_3 shows reduced ductility and fracture toughness. Notably, the fracture toughness of WCrY at 1000 °C exhibits greater variation compared to the others, as this temperature marks the onset of stable crack growth.

Interestingly, oxide particles are predominantly found at the grain boundaries of Y_2O_3-doped WCr alloy, unlike in other materials doped with Y_2O_3, such as Eurofer 97 [74,75], pure W [36], and tungsten-heavy alloys [76], where yttria nanoparticles are homogeneously dispersed within grains. A more homogeneous distribution of oxide particles within the grain interior is generally considered more beneficial than their preferential presence at grain boundaries. Intragranular yttria dispersoids have been reported to provide a more significant strengthening effect than intergranular ones [37], and a reduced presence of intergranular particles may improve the toughness of the material by reducing stress concentration and, thus, fracture initiation at grain boundaries. However, incorporating oxide particles into the WCr grain interior is currently not feasible, as shown in this work through ball milling and FAST manufacturing routes, either doped with yttrium or yttria.

4. Conclusions

This study examined the microstructure and performance of Y_2O_3-doped WCr alloy in comparison with Y-doped WCr for first wall applications. Microstructural analysis revealed a greater variety of oxides located at grain boundaries in as-sintered WCr-Y_2O_3, including Y_2O_3 as intentionally added, Cr-O, and Y-Cr-O particles, which are likely formed during sintering. In contrast, predominantly Y-O particles were detected in as-sintered WCrY. WCr-Y_2O_3 exhibits slightly larger average grain and particle sizes compared to WCrY. Regarding oxidation resistance under humid synthetic air at 1000 °C, WCr-Y_2O_3 demonstrated a halved linear oxidation rate compared to WCrY. This enhanced oxidation resistance was attributed to a more effective REE in WCr-Y_2O_3. Y-containing particles are uniformly distributed on the chromia protective scale in oxidized WCr-Y_2O_3, and the inner oxide layer underneath shows decreased thickness compared to oxidized WCrY. Further investigation is required to understand the oxidation mechanisms responsible for the distinct surface morphologies observed between WCr-Y_2O_3 and WCrY. Thermal-mechanical tests indicated that WCr-Y_2O_3 exhibited higher flexural strength, particularly at low temperatures where it remained $\geq$1 GPa. At temperatures above 600 °C, the flexural strength of WCr-Y_2O_3 was still 70–160 MPa higher than that of WCrY. However, WCr-Y_2O_3 displayed overall lower fracture toughness (~50% less) than WCrY. Economically, the use of reactive element oxides instead of elemental forms offers a cost-effective alternative in manufacturing SMART materials, which is an important aspect for mass production [77]. This work highlights Y_2O_3 as a promising alternative additive to Y in WCr alloys.

Author Contributions: Conceptualization, J.C. and A.L.; methodology, J.C., E.T. and A.L.; formal analysis, J.C., M.R. and E.T.; investigation, J.C., E.T., M.R. and D.N.-M.; writing—original draft preparation, J.C.; writing—review and editing, E.T., A.L., D.N.-M., E.P., T.W. and J.G.-J.; supervision, A.L. and J.G.-J.; project administration, A.L., J.Y.P., M.B., J.W.C. and C.L. All authors have read and agreed to the published version of the manuscript.

Funding: This work has been carried out within the framework of the EUROfusion Consortium, funded by the European Union via the Euratom Research and Training Programme (Grant Agreement No 101052200—EUROfusion). Views and opinions expressed are, however, those of the author(s) only and do not necessarily reflect those of the European Union or the European Commission. Neither the European Union nor the European Commission can be held responsible for them. J.C. acknowledges the financial support of the China Scholarship Council (CSC). The authors acknowledge Ralf Steinert from IMD-2, Forschungszentrum Jülich GmbH, Germany, for his assistance and instruction with the FAST sintering process. CIME-UPM activities were supported by the Spanish "Agencia Estatal de Investigación" under the call "Proyectos de Generación de Conocimiento 2022" (3DPOSTHERMEC, PID2022-137274NB-C33PID). D.N.M., E.P., and T.W. also acknowledge funding by the EPSRC Energy Programme [grant number EP/W006839/1]. All authors have read and agreed to the published version of the manuscript.

Data Availability Statement: The raw data supporting the conclusions of this article will be made available by the authors on request.

Conflicts of Interest: Authors Jie Chen, Marcin Rasiński, Andrey Litnovsky, Martin Bram, Jan Willem Coenen, Christian Linsmeier and Jesus Gonzalez-Julian were employed by the company Forschungszentrum Jülich GmbH. The remaining authors declare that the research was conducted in the absence of any commercial or financial relationships that could be construed as a potential conflict of interest.

References

1. Smid, I.; Akiba, M.; Vieider, G.; Plöchl, L. Development of tungsten armor and bonding to copper for plasma-interactive components. *J. Nucl. Mater.* **1998**, *258–263*, 160–172. [CrossRef]
2. Maisonnier, D.; Cook, I.; Sardain, P.; Andreani, R.; Di Pace, L.; Forrest, R.; Giancarli, L.; Hermsmeyer, S.; Norajitra, P.; Taylor, N.; et al. *A Conceptual Study of Commercial Fusion Power Plants. Final Report of the European Fusion Power Plant Conceptual Study (PPCS)*; EFDA report number EFDA (05)-27/4.10; EFDA: Addis Ababa, Ethiopia, 2005; Volume 1.
3. Wegener, T.; Klein, F.; Litnovsky, A.; Rasinski, M.; Brinkmann, J.; Koch, F.; Linsmeier, C. Development of yttrium-containing self-passivating tungsten alloys for future fusion power plants. *Nucl. Mater. Energy* **2016**, *9*, 394–398. [CrossRef]
4. Litnovsky, A.; Klein, F.; Tan, X.; Ertmer, J.; Coenen, J.W.; Linsmeier, C.; Gonzalez-Julian, J.; Bram, M.; Povstugar, I.; Morgan, T.; et al. Advanced Self-Passivating Alloys for an Application under Extreme Conditions. *Metals* **2021**, *11*, 1255. [CrossRef]
5. Koch, F.; Bolt, H. Self passivating W-based alloys as plasma facing material for nuclear fusion. *Phys. Scr.* **2007**, *T128*, 100–105. [CrossRef]
6. Zhu, H.; Tan, X.; Tu, Q.; Mao, Y.; Shu, Z.; Chen, J.; Luo, L.; Litnovsky, A.; Coenen, J.W.; Linsmeier, C.; et al. Effect of Pressure on Densification and Microstructure of W-Cr-Y-Zr Alloy during SPS Consolidated at 1000 °C. *Metals* **2022**, *12*, 1437. [CrossRef]
7. Xiong, Z.; Ma, W.; Deng, Z.; Dong, D. Strong yet ductile self-passivating W-10Cr alloy by laser powder bed fusion. *Int. J. Refract. Met. Hard Mater.* **2023**, *116*, 106365. [CrossRef]
8. Wang, W.; Tan, X.; Yang, S.; Mao, Y.; Luo, L.; Zhu, X.; Litnovsky, A.; Coenen, J.; Linsmeier, C.; Wu, Y. The influence of powder characteristics on densification behavior and microstructure evolution of W-Cr-Zr alloy consolidated by field-assisted sintering technology. *Int. J. Refract. Met. Hard Mater.* **2022**, *108*, 105939. [CrossRef]
9. Wang, W.; Tan, X.; Yang, S.; Luo, L.; Zhu, X.; Mao, Y.; Litnovsky, A.; Coenen, J.; Linsmeier, C.; Wu, Y. On grain growth and phase precipitation behaviors during W-Cr-Zr alloy densification using field-assisted sintering technology. *Int. J. Refract. Met. Hard Mater.* **2021**, *98*, 105552. [CrossRef]
10. Wang, Y.; Harutyunyan, Z.; Gasparyan, Y.; Ogorodnikova, O.; Sinelnikov, D.; Efimov, N.; Tan, X.; Umerenkova, A.; Grishaev, M. Annealing effect on deuterium retention in W-Cr-Y alloy. *J. Nucl. Mater.* **2024**, *593*, 154975. [CrossRef]
11. Harutyunyan, Z.; Gasparyan, Y.; Efimov, V.; Litnovsky, A.; Klein, F.; Pisarev, A.; Coenen, J.W.; Linsmeier, C. Analysis of trapping sites for deuterium in W–Cr–Y SMART alloy. *Vacuum* **2022**, *199*, 110956. [CrossRef]
12. Harutyunyan, Z.; Ogorodnikova, O.; Gasparyan, Y.; Umerenkova, A.; Wang, Y.; Sal, E.; García-Rosales, C. Deuterium retention in W-Cr-Y alloy: Impact of the manufacturing method and helium presence. *J. Nucl. Mater.* **2023**, *578*, 154353. [CrossRef]
13. Terentyev, D.; Jenus, P.; Sal, E.; Zinovev, A.; Chang, C.-C.; Garcia-Rosales, C.; Kocen, M.; Novak, S.; Van Renterghem, W. Development of irradiation tolerant tungsten alloys for high temperature nuclear applications. *Nucl. Fusion* **2022**, *62*, 086035. [CrossRef]
14. Veverka, J.; Vilémová, M.; Lukáč, F.; Kądzielawa, A.P.; Legut, D.; Vontorová, J.; Kozlík, J.; Chráska, T. Decreasing the W-Cr solid solution decomposition rate: Theory, modelling and experimental verification. *J. Nucl. Mater.* **2023**, *576*, 154288. [CrossRef]
15. Qian, Y.; Gilbert, M.R.; Dezerald, L.; Nguyen-Manh, D.; Cereceda, D. Ab initio study of tungsten-based alloys under fusion power-plant conditions. *J. Nucl. Mater.* **2023**, *581*, 154422. [CrossRef]
16. Kirillova, V.; Popov, N.; Gurova, J.; Bachurina, D.; Tan, X.; Fedotov, I.; Suchkov, A. Brazing SMART tungsten alloys to RAFM steels by Titanium-Zirconium-Beryllium brazing alloy. *Fusion Eng. Des.* **2024**, *201*, 114297. [CrossRef]

17. Efimov, N.; Sinelnikov, D.; Kolodko, D.; Grishaev, M.; Nikitin, I. On the reconstruction of LEIS spectra after distortion by an electrostatic energy analyzer. *Appl. Surf. Sci.* **2024**, *676*, 161006. [CrossRef]
18. Efimov, N.; Sinelnikov, D.; Grishaev, M.; Nikitin, I.; Wang, Y.; Harutyunyan, Z.; Gasparyan, Y. On the possibility of quantitative W-Cr-Y analysis by grazing ion-surface scattering spectroscopy. *Nucl. Instrum. Methods Phys. Res. Sect. B Beam Interact. Mater. At.* **2024**, *546*, 165177. [CrossRef]
19. Calvo, A.; García-Rosales, C.; Ordás, N.; Iturriza, I.; Schlueter, K.; Koch, F.; Pintsuk, G.; Tejado, E.; Pastor, J.Y. Self-passivating W-Cr-Y alloys: Characterization and testing. *Fusion Eng. Des.* **2017**, *124*, 1118–1121. [CrossRef]
20. Chen, S.; Xue, L.; Yin, S.; Yan, Y.; Zhou, Q. Microstructures and Antioxidation of W Self-Passivating Alloys: Synergistic Effect of Yttrium and Milling Time. *Metals* **2024**, *14*, 194. [CrossRef]
21. Ye, C.; Chen, S.; Liu, W.; Xue, L.; Yin, S.; Yan, Y. Effects of Yttrium on High Temperature Oxidation Resistance of W-Si-Y Self-Passivating Alloys. *Metals* **2022**, *12*, 2040. [CrossRef]
22. Hou, P.Y. 1.10—Oxidation of Metals and Alloys. In *Shreir's Corrosion*; Cottis, B., Ed.; Elsevier: Oxford, UK, 2010; pp. 195–239.
23. Fritscher, K. The Reactive Element Effect. *Metall. Mater. Trans. A* **2023**, *54*, 64–74. [CrossRef]
24. Stringer, J.; Wilcox, B.A.; Jaffee, R.I. The high-temperature oxidation of nickel-20 wt. % chromium alloys containing dispersed oxide phases. *Oxid. Met.* **1972**, *5*, 11–47. [CrossRef]
25. Quadakkers, W.J.; Holzbrecher, H.; Briefs, K.G.; Beske, H. Differences in growth mechanisms of oxide scales formed on ODS and conventional wrought alloys. *Oxid. Met.* **1989**, *32*, 67–88. [CrossRef]
26. Whittle, D.P.; Stringer, J. Improvements in high temperature oxidation resistance by additions of reactive elements or oxide dispersions. *Philos. Trans. R. Soc. London. Ser. A Math. Phys. Sci.* **1980**, *295*, 309–329.
27. Klein, F.; Wegener, T.; Litnovsky, A.; Rasinski, M.; Tan, X.; Gonzalez-Julian, J.; Schmitz, J.; Bram, M.; Coenen, J.; Linsmeier, C. Oxidation resistance of bulk plasma-facing tungsten alloys. *Nucl. Mater. Energy* **2018**, *15*, 226–231. [CrossRef]
28. Calvo, A.; Schlueter, K.; Tejado, E.; Pintsuk, G.; Ordás, N.; Iturriza, I.; Neu, R.; Pastor, J.; García-Rosales, C. Self-passivating tungsten alloys of the system W-Cr-Y for high temperature applications. *Int. J. Refract. Met. Hard Mater.* **2018**, *73*, 29–37. [CrossRef]
29. Wang, W.; Tan, X.; Liu, J.; Chen, X.; Wu, M.; Luo, L.; Zhu, X.; Chen, H.; Mao, Y.; Litnovsky, A.; et al. The influence of heating rate on W-Cr-Zr alloy densification process and microstructure evolution during spark plasma sintering. *Powder Technol.* **2020**, *370*, 9–18. [CrossRef]
30. Calvo, A.; García-Rosales, C.; Koch, F.; Ordás, N.; Iturriza, I.; Greuner, H.; Pintsuk, G.; Sarbu, C. Manufacturing and testing of self-passivating tungsten alloys of different composition. *Nucl. Mater. Energy* **2016**, *9*, 422–429. [CrossRef]
31. Vilémová, M.; Illková, K.; Lukáč, F.; Matějíček, J.; Klečka, J.; Leitner, J. Microstructure and phase stability of W-Cr alloy prepared by spark plasma sintering. *Fusion Eng. Des.* **2018**, *127*, 173–178. [CrossRef]
32. Pint, B.A.; Wright, I.G. Oxidation Behavior of ODS Fe–Cr Alloys. *Oxid. Met.* **2005**, *63*, 193–213. [CrossRef]
33. Quadakkers, W. Oxidation of ODS alloys. *J. Phys. IV* **1993**, *3*, C9-177–C9-186. [CrossRef]
34. Ramanarayanan, T.A.; Ayer, R.; Petkovic-Luton, R.; Leta, D.P. The influence of yttrium on oxide scale growth and adherence. *Oxid. Met.* **1988**, *29*, 445–472. [CrossRef]
35. Dong, Z.; Ma, Z.; Yu, L.; Liu, Y. Achieving high strength and ductility in ODS-W alloy by employing oxide@W core-shell nanopowder as precursor. *Nat. Commun.* **2021**, *12*, 5052. [CrossRef] [PubMed]
36. Yao, G.; Liu, X.; Zhao, Z.; Luo, L.; Cheng, J.; Zan, X.; Wang, Z.; Xu, Q.; Wu, Y. Excellent performance of W–Y_2O_3 composite via powder process improvement and Y_2O_3 refinement. *Mater. Des.* **2021**, *212*, 110249. [CrossRef]
37. Wang, M.; Sun, H.; Pang, B.; Xi, X.; Nie, Z. Structure evolution of Y_2O_3 and consequent effects on mechanical properties of W–Y_2O_3 alloy prepared by ball milling and SPS. *Mater. Sci. Eng. A* **2022**, *832*, 142448. [CrossRef]
38. Li, L.; Dong, Z.; Ma, Z.; Liu, C.; Yu, L.; Liu, Y. Ultrahigh strength and toughness in W-Y_2O_3 alloy with bimodal and lamellar structures. *Mater. Res. Lett.* **2023**, *11*, 439–445. [CrossRef]
39. Sobieraj, D.; Wróbel, J.S.; Gilbert, M.R.; Litnovsky, A.; Klein, F.; Kurzydłowski, K.J.; Nguyen-Manh, D. Composition Stability and Cr-Rich Phase Formation in W-Cr-Y and W-Cr-Ti Smart Alloys. *Metals* **2021**, *11*, 743. [CrossRef]
40. Sobieraj, D.; Wróbel, J.S.; Gilbert, M.R.; Kurzydłowski, K.J.; Nguyen-Manh, D. Co-segregation of Y and Zr in W-Cr-Y-Zr alloys: First-principles modeling at finite temperature and application to SMART materials. *J. Alloy. Met. Syst.* **2023**, *2*, 100011. [CrossRef]
41. Sublet, J.-C.; Eastwood, J.; Morgan, J.; Gilbert, M.; Fleming, M.; Arter, W. FISPACT-II: An advanced simulation system for activation, transmutation and material modelling. *Nucl. Data Sheets* **2017**, *139*, 77–137. [CrossRef]
42. Schneider, C.A.; Rasband, W.S.; Eliceiri, K.W. NIH Image to ImageJ: 25 years of image analysis. *Nat. Methods* **2012**, *9*, 671–675. [CrossRef]
43. Guinea, G.V.; Pastor, J.Y.; Planas, J.; Elices, M. Stress intensity factor, compliance and CMOD for a general three-point-bend beam. *Int. J. Fract.* **1998**, *89*, 103–116. [CrossRef]
44. Pastor, J.Y.; Guinea, G.; Planas, J.; Elices, M. Nueva expresión del factor de intensidad de tensiones para la probeta de flexión en tres puntos. *An. Mecánica Fract.* **1995**, *12*, 85–90.
45. Dou, P.; Qiu, L.; Jiang, S.; Kimura, A. Crystal and metal/oxide interface structures of nanoparticles in Fe–16Cr–0.1Ti–0.35Y_2O_3 ODS steel. *J. Nucl. Mater.* **2019**, *523*, 320–332. [CrossRef]
46. Kresse, G.; Joubert, D. From ultrasoft pseudopotentials to the projector augmented-wave method. *Phys. Rev. B* **1999**, *59*, 1758–1775. [CrossRef]

47. Kresse, G.; Furthmüller, J. Efficient iterative schemes for ab initio total-energy calculations using a plane-wave basis set. *Phys. Rev. B* **1996**, *54*, 11169. [CrossRef]
48. Kresse, G.; Furthmüller, J. Efficiency of ab-initio total energy calculations for metals and semiconductors using a plane-wave basis set. *Comput. Mater. Sci.* **1996**, *6*, 15–50. [CrossRef]
49. Karpinos, D.M.; Listovnichaya, S.P.; Balakhnina, V.N.; Okunevskii, Y.N. Reaction between thin yttrium oxide and chromium films in the presence of oxygen. *Sov. Powder Met. Met. Ceram.* **1979**, *18*, 668–671. [CrossRef]
50. Pasebani, S.; Dutt, A.K.; Burns, J.; Charit, I.; Mishra, R.S. Oxide dispersion strengthened nickel based alloys via spark plasma sintering. *Mater. Sci. Eng. A* **2015**, *630*, 155–169. [CrossRef]
51. de Castro, V.; Marquis, E.; Lozano-Perez, S.; Pareja, R.; Jenkins, M. Stability of nanoscale secondary phases in an oxide dispersion strengthened Fe–12Cr alloy. *Acta Mater.* **2011**, *59*, 3927–3936. [CrossRef]
52. Tang, C.; Pan, F.; Qu, X.; Jia, C.; Duan, B.; He, X. Spark plasma sintering cobalt base superalloy strengthened by Y–Cr–O compound through high-energy milling. *J. Mech. Work. Technol.* **2008**, *204*, 111–116. [CrossRef]
53. Mao, Z.; Xiong, L.; Liu, S. The formation of the complex oxide in Ni-based alloy powder during mechanical milling and heat treatment. *J. Alloys Compd.* **2021**, *879*, 160333. [CrossRef]
54. Chevalier, S.; Larpin, J. Formation of perovskite type phases during the high temperature oxidation of stainless steels coated with reactive element oxides. *Acta Mater.* **2002**, *50*, 3107–3116. [CrossRef]
55. Zhang, H.; Gorley, M.J.; Chong, K.B.; Fitzpatrick, M.E.; Roberts, S.G.; Grant, P.S. An in situ powder neutron diffraction study of nano-precipitate formation during processing of oxide-dispersion-strengthened ferritic steels. *J. Alloys Compd.* **2014**, *582*, 769–773. [CrossRef]
56. Kim, B.; Jang, J.; Kim, T.K.; Ahn, J.H. Formation of Nano-Sized Y_2O_3 Dispersoids in Mechanically Alloyed Ni–(Cr, Y_2O_3, Y) Alloys During Heat-Treatments. *J. Nanosci. Nanotechnol.* **2012**, *12*, 5510–5513. [CrossRef] [PubMed]
57. Xu, H.; Chen, M.; Cheng, K.; Zhang, L.; Du, Y. Thermodynamic modeling of the chromium-yttrium-oxygen system. *Calphad* **2019**, *64*, 1–10. [CrossRef]
58. Robino, C.V. Representation of mixed reactive gases on free energy (Ellingharn-Richardson) diagrams. *Met. Mater. Trans. B* **1996**, *27*, 65–69. [CrossRef]
59. Flower, H.; Gould, P.; Moon, D.; Tuson, A. The oxidation of chromium. In *Microscopy of Oxidation*; CRC Press: Boca Raton, FL, USA, 2023; pp. 98–112.
60. Pujilaksono, B.; Jonsson, T.; Halvarsson, M.; Panas, I.; Svensson, J.E.; Johansson, L.G. Paralinear Oxidation of Chromium in O_2 + H_2O Environment at 600–700 °C. *Oxid. Met.* **2008**, *70*, 163–188. [CrossRef]
61. Schmid, B.; Aas, N.; Grong, Ø.; Ødegård, R. High-temperature oxidation of nickel and chromium studied with an in-situ environmental scanning electron microscope. *Scanning* **2001**, *23*, 255–266. [CrossRef]
62. Klein, F.; Litnovsky, A.; Wegener, T.; Tan, X.; Gonzalez-Julian, J.; Rasinski, M.; Schmitz, J.; Linsmeier, C.; Bram, M.; Coenen, J.W. Sublimation of advanced tungsten alloys under DEMO relevant accidental conditions. *Fusion Eng. Des.* **2019**, *146*, 1198–1202. [CrossRef]
63. Li, X.; He, S.; Liang, J.; Zhou, X. High-Temperature Oxidation Behavior and Oxide Scale Structure of Yttrium-Modified Ni–16Mo–7Cr–4Fe Superalloy at 1273 K. *Oxid. Met.* **2019**, *92*, 67–88. [CrossRef]
64. Seybolt, A. High temperature oxidation of chromium containing Y_2O_3. *Corros. Sci.* **1966**, *6*, 263–269. [CrossRef]
65. Hou, P.Y.; Stringer, J. The influence of ion-implanted yttrium on the selective oxidation of chromium in Co-25 wt.% Cr. *Oxid. Met.* **1988**, *29*, 45–73. [CrossRef]
66. Przybylski, K.; Yurek, G.J. The Influence of Implanted Yttrium on the Microstructures of Chromia Scales Formed on a Co-45 Weight Percent Cr Alloy. *J. Electrochem. Soc.* **1988**, *135*, 517–523. [CrossRef]
67. Molin, S.; Persson, Å.; Skafte, T.; Smitshuysen, A.; Jensen, S.; Andersen, K.; Xu, H.; Chen, M.; Hendriksen, P. Effective yttrium based coating for steel interconnects of solid oxide cells: Corrosion evaluation in steam-hydrogen atmosphere. *J. Power Sources* **2019**, *440*, 226814. [CrossRef]
68. Pillis, M.F.; Correa, O.V.; Ramanathan, L.V. High temperature oxidation behavior of yttrium dioxide coated Fe-20Cr alloy. *Mater. Res.* **2016**, *19*, 611–617. [CrossRef]
69. Stott, F.H.; Wood, G.C.; Stringer, J. The influence of alloying elements on the development and maintenance of protective scales. *Oxid. Met.* **1995**, *44*, 113–145. [CrossRef]
70. Saito, Y.; Önay, B.; Maruyama, T. The reactive element effect (REE) in oxidation of alloys. *J. Phys. Iv* **1993**, *3*, C9-217–C9-230. [CrossRef]
71. Liu, R.; Xie, Z.; Fang, Q.; Zhang, T.; Wang, X.; Hao, T.; Liu, C.; Dai, Y. Nanostructured yttria dispersion-strengthened tungsten synthesized by sol–gel method. *J. Alloys Compd.* **2015**, *657*, 73–80. [CrossRef]
72. Liu, G.; Zhang, G.J.; Jiang, F.; Ding, X.D.; Sun, Y.J.; Sun, J.; Ma, E. Nanostructured high-strength molybdenum alloys with unprecedented tensile ductility. *Nat. Mater.* **2013**, *12*, 344–350. [CrossRef]
73. Gurland, J.; Plateau, J. *The Mechanism of Ductile Rupture of Metals Containing Inclusions*; Brown Univ., Providence; Institut de Recherches de la Siderugie: St.-Germain-en-Laye, France, 1963.
74. Klimiankou, M.; Lindau, R.; Möslang, A. HRTEM Study of yttrium oxide particles in ODS steels for fusion reactor application. *J. Cryst. Growth* **2003**, *249*, 381–387. [CrossRef]

75. Lindau, R.; Möslang, A.; Schirra, M.; Schlossmacher, P.; Klimenkov, M. Mechanical and microstructural properties of a hipped RAFM ODS-steel. *J. Nucl. Mater.* **2002**, *307–311*, 769–772. [CrossRef]
76. Lee, K.H.; Cha, S.I.; Ryu, H.J.; Hong, S.H. Effect of two-stage sintering process on microstructure and mechanical properties of ODS tungsten heavy alloy. *Mater. Sci. Eng. A* **2007**, *458*, 323–329. [CrossRef]
77. Litnovsky, A.; Chen, J.; Bram, M.; Gonzalez-Julian, J.; Zoz, H.; Benz, H.U.; Huber, J.; Pintsuk, G.; Coenen, J.W.; Linsmeier, C. SMART materials for DEMO: Towards industrial production. *Fusion Eng. Des.* **2024**, *203*, 114423. [CrossRef]